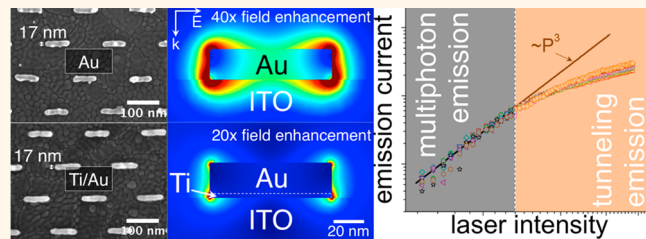


High-Yield, Ultrafast, Surface Plasmon-Enhanced, Au Nanorod Optical Field Electron Emitter Arrays

Richard G. Hobbs,^{†,‡} Yujia Yang,^{†,‡} Arya Fallahi,[‡] Philip D. Keathley,[†] Eva De Leo,^{†,||} Franz X. Kärtner,^{†,‡} William S. Graves,[§] and Karl K. Berggren^{*,†}

[†]Research Laboratory of Electronics, Massachusetts Institute of Technology, Cambridge, Massachusetts 02139, United States, [‡]Center for Free-Electron Laser Science, Deutsches Elektronen-Synchrotron, Hamburg 22761, Germany, and [§]Nuclear Reactor Laboratory, Massachusetts Institute of Technology, Cambridge, Massachusetts 02139, United States. ^{||}These authors contributed equally to this work. ^{||}Present address: Optical Materials Engineering Laboratory, ETH Zurich, 8092 Zurich, Switzerland.

ABSTRACT Here we demonstrate the design, fabrication, and characterization of ultrafast, surface-plasmon enhanced Au nanorod optical field emitter arrays. We present a quantitative study of electron emission from Au nanorod arrays fabricated by high-resolution electron-beam lithography and excited by 35 fs pulses of 800 nm light. We present accurate models for both the optical field enhancement of Au nanorods within high-density arrays, and electron emission from those nanorods. We have also studied the effects of surface plasmon damping induced by metallic interface layers at the substrate/nanorod interface on near-field enhancement and electron emission. We have identified the peak optical field at which the electron emission mechanism transitions from a 3-photon absorption mechanism to strong-field tunneling emission. Moreover, we have investigated the effects of nanorod array density on nanorod charge yield, including measurement of space-charge effects. The Au nanorod photocathodes presented in this work display 100–1000 times higher conversion efficiency relative to previously reported UV triggered emission from planar Au photocathodes. Consequently, the Au nanorod arrays triggered by ultrafast pulses of 800 nm light in this work may outperform equivalent UV-triggered Au photocathodes, while also offering nanostructuring of the electron pulse produced from such a cathode, which is of interest for X-ray free-electron laser (XFEL) development where nanostructured electron pulses may facilitate more efficient and brighter XFEL radiation.



KEYWORDS: plasmons · nanorods · nano-optics · ultrafast electron emission · strong-field tunneling · field-enhancement · lightwave electronics

Nanoparticles exhibiting localized surface plasmon resonances (LSPR) are useful for nano-optics applications that require optical-field enhancement. The local enhancement of optical fields at the nanoscale by the collective oscillation of electrons (plasmons) in such particles when illuminated at resonant wavelengths enables the use of these particles for surface-enhanced Raman spectroscopy,¹ high-resolution imaging,² nanochemistry,³ metamaterials,^{4–6} sensor,^{7–9} optoelectronics,¹⁰ nanolithography,¹¹ and photocathode¹² applications. Plasmonic nanoparticle arrays are of particular interest for use as ultrafast, high-brightness photoelectron emitters in next-generation X-ray free-electron lasers (XFELs) enabling ultrafast X-ray imaging, and diffraction, as well as

time-resolved electron microscopy and spectroscopy experiments.

XFELs, as well as other electron-emission applications, depend critically on photocathode performance. Metallic photocathodes for example are desirable due to their relative insensitivity to contamination, which allows their operation under poorer vacuum conditions than high-efficiency alkali halides. As such, there has been a drive to improve the efficiency of metallic photocathodes such as Au and Cu.^{13–15} Moreover, the performance of XFELs relies on the ability to first generate nanometer scale density modulations in the electron beam, which can then be used to coherently emit X-rays.^{16–18} A compact coherent X-ray source based on a modulated electron beam produced by a nanostructured

* Address correspondence to berggren@mit.edu.

Received for review August 16, 2014 and accepted November 7, 2014.

Published online November 07, 2014
10.1021/nn504594g

© 2014 American Chemical Society

photocathode has been recently proposed.¹⁹ Consequently, the development of nanostructured photocathodes is key to improving next-generation ultrafast, coherent X-ray sources.

Electron emission has previously been demonstrated from arrays of plasmonic nanoparticles and nanostructured plasmonic surfaces.^{12–14,20,21} Dombi *et al.* and Nagel *et al.* have both demonstrated electron emission and acceleration within the surface-plasmon-enhanced near-field of plasmonic particles lying in-, and out-of-plane of the substrate, respectively. Douillard *et al.* have also previously investigated electron emission from multipolar plasmonic particles by photoemission electron microscopy (PEEM). Prior work on ultrafast photoemission from plasmonic nanoparticle arrays focused on the energy spectra of electrons produced from such particles, rather than the quantitative charge-yield. Additionally, the nanoparticles studied were of dimensions significantly larger than those studied in the present work. Furthermore, while quantitative studies of charge-yield from plasmonic Au photocathodes have been performed recently,¹⁴ they were restricted to a range of laser intensities where the emission mechanism lay firmly within the multiphoton absorption regime. Thus, a quantitative investigation of photocathode performance in the strong-field regime is presently lacking.

In this work we will further advance the field of ultrafast plasmonic photocathodes by (1) scaling the critical dimensions of the emitters, fabricated by high-resolution electron-beam lithography, into the sub-20 nm regime; (2) investigating the effects of substrate, and traditional adhesion-promoting layers such as Ti, on charge yield from overlying Au nanorods; and (3) studying effects of laser intensity, applied DC field, angle of linear polarization, and nanorod array density on charge yield.

Fabrication of Au nanorods with sub-20 nm critical dimensions will allow greater localization of the electron emission site, which is of interest for creating nanostructured electron beams as discussed above. Investigation of the effect of the Au/substrate interface on electron emission from arrays of plasmonic Au nanorods prepared by electron-beam lithography will also be key to optimizing the efficiency of such electron sources. The existence of a substrate not only shifts the spectral position of the Au nanorod LSPR, but also modifies the optical near-field distribution due to mode hybridization.²² Higher index substrates lead to a more pronounced red-shift of the LSPR, and stronger field localization at the interface between the plasmonic nanostructure and substrate.^{23–27} A strong optical field enhancement at the nanorod/vacuum interface rather than the nanorod/substrate interface is preferred for photocathode applications to reduce electron scattering from the substrate; thus, a low-index, electrically conductive substrate, is preferred.

Moreover, the effects of conventional adhesion-promoting metals such as Ti, used in the preparation of Au nanorods by electron-beam lithography, on photoelectron yield are worthy of investigation. Previously, such metallic layers have been shown to reduce the Q-factor of the LSPR within overlying Au nanorods due to increased damping of the resonance.²⁸ Lastly, the scaling of emission current as a function of nanorod array density, laser-intensity and applied anode bias will be key to understanding the factors affecting charge-yield from plasmonic photocathodes, such as space-charge, electron emission mechanism and optical field enhancement. A better understanding of the factors affecting charge-yield from these photocathodes may then allow us to generate more efficient electron sources for next-generation, ultrafast metrology.

RESULTS AND DISCUSSION

Here, we show how a Ti adhesion layer affects optical near-field enhancement, and hence affects photocathode performance. Figure 1 shows SEM images, results of near-field simulations, optical extinction spectra and photoemission measurements, for plasmonic Au nanorod arrays with sub-20 nm critical dimensions, fabricated both with and without a Ti adhesion-promoting layer.

Figure 1a shows SEM images of high-density Au nanorod arrays, prepared with and without a Ti adhesion layer on an indium-doped tin oxide (ITO)-coated sapphire substrate. Details of nanorod array fabrication are available in the methods section in the Supporting Information. The image highlights our ability to fabricate nanorods with dimensions in the sub-20 nm regime in the absence of an adhesion-promoting layer such as Ti.

Figure 1b shows the results of simulations of near-field enhancement in the vicinity of a Au nanorod on an ITO substrate both with, and without, a Ti adhesion-layer (see Supporting Information for details about the simulations). The results clearly show a stronger near-field enhancement for the case of Ti-free Au nanorods. An ITO substrate was selected for this work due to its low index and relatively high electrical conductivity (substrate selection is discussed in further detail in the Supporting Information). The simulated field-enhancement spectra (Figure 1c) show that the peak field-enhancement for a Ti-free Au nanorod is approximately twice that of a Au nanorod with a Ti layer. Additionally, the simulated optical power absorption spectra (Supporting Information Figure S6) show that when a Ti layer is present, it dissipates 75% of the total absorbed power. Moreover, the power absorption in Au is significantly higher in the absence of a Ti layer. Broadening of the LSPR peak in Supporting Information Figure S6 is also an indication of Ti-induced damping of the LSPR. Thus, removal of the Ti layer and fabrication of Au nanorods directly on an ITO substrate should lead to improved charge yield

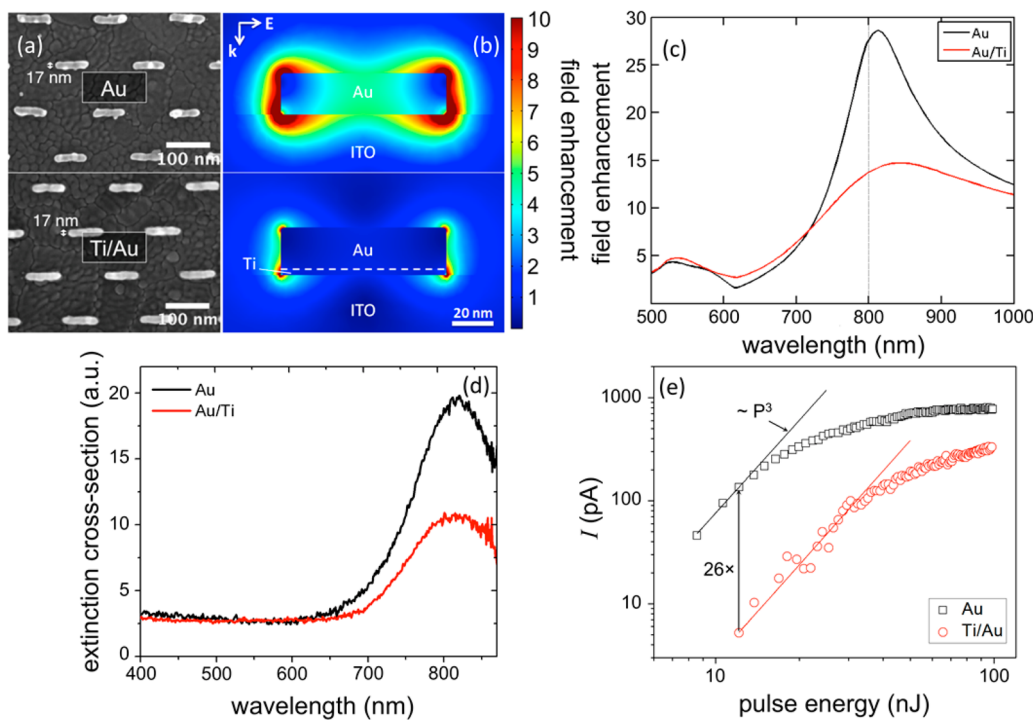


Figure 1. (a) SEM images of Au nanorods prepared without (top) and with (bottom) a 3 nm Ti adhesion layer on 80 nm ITO on a Si substrate. (b) Cross section of simulated spatial distribution of near-field enhancement at Au nanorods, directly on ITO (top), and with a Ti adhesion layer (bottom) (color scale is saturated). (c) Simulated field-enhancement spectra for Au nanorods prepared with (red line) and without (black line) a Ti layer. Vertical gray line represents the central wavelength of the drive-laser (800 nm, fwhm 50 nm). (d) Optical extinction spectra acquired for a 200 nm pitch array of Au nanorods prepared with (red line) and without (black line) a 3 nm Ti adhesion promotion layer. The spectra show a doubling of the extinction for Au nanorods prepared without Ti. (e) Log–log plot of emission current vs pulse energy with an applied anode bias of +1 kV, for a 400 nm pitch square array of Au nanorods, prepared without (open black squares) and with (open red circles) a Ti adhesion layer. Both arrays display emission current scaling with the 3rd power of laser pulse-energy (intensity) for low values of pulse-energy, as indicated by the color coordinated lines overlain on each data set. At 12.1 nJ the emission current from the Au nanorod array is 26 times that of the Ti/Au nanorod array as indicated on the plot.

and quantum efficiency due to reduced damping of the LSPR. Notably, the measured (Figure 1d) and simulated absorption spectra for the Au nanorod arrays studied in this work display broad bandwidths (~ 100 nm), which may thus support shorter optical pulses than the 35 fs (40 nm bandwidth) pulses used here, and consequently may be of interest for production of sub-10 fs electron pulses.

Figure 1d shows optical extinction spectra acquired for 200 nm pitch arrays of Au nanorods prepared with (red line), and without (black line), a Ti adhesion promotion layer. The presence of a 3 nm Ti layer led to a halving of the optical extinction. Assuming that the extinction cross-section is proportional to the optical intensity, or equivalently the square of the optical field, then a 4-fold reduction in the extinction cross-section would have been expected based on the peak-field simulation results shown in Figure 1c. Possible causes for the discrepancy between simulation and experiment include the fact that the Ti deposited in the experiment is likely to contain a significant amount of oxygen, thus reducing damping of the surface plasmon resonance with respect to pure Ti metal, which was used in the simulation. A reduction in plasmon damping would result in a greater optical

field enhancement and thus an increased optical extinction cross-section. Moreover, the simulation results in Figure 1c are representative of the peak optical field at the nanorod apexes, however, the integrated field over the entire rod would be more representative of the contribution to optical extinction. Figure 1e shows a log–log plot of emission current vs laser pulse-energy for nanorod arrays prepared with, and without Ti. We have consistently observed enhanced emission from Au nanorod arrays prepared without an additional metallic adhesion promoter such as Ti. The results shown in Figure 1e demonstrate a 26-fold increase in emission current, at an incident pulse-energy of 12.1 nJ, for a 400 nm pitch square array of Ti-free Au nanorods, compared to an identical array prepared with a 5 nm Ti layer. The log–log plot of emission current vs pulse-energy shows that both arrays display a slope commensurate with a 3-photon process at 12.1 nJ. The observed 26-fold increase in emission current thus suggests that the optical field is enhanced 1.7 times more by Ti-free Au rods than equivalent TiAu nanorods, which is in good agreement with the predicted doubling of field-enhancement from the simulation results shown in Figure 1c. Figure 1e also shows that the emission current deviates

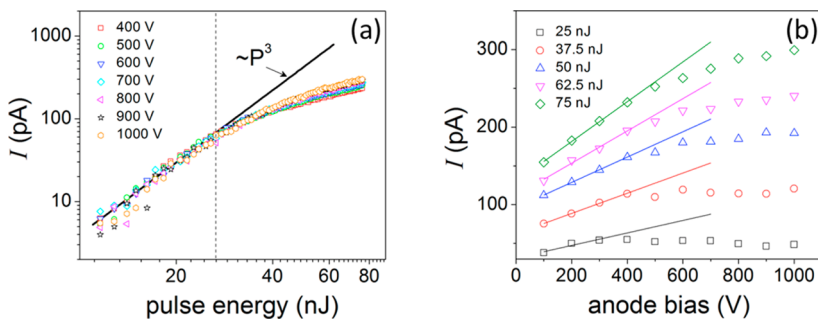


Figure 2. (a) Log–log plot of emission current vs pulse energy (P) for a $1\text{ }\mu\text{m}$ pitch square array of Au nanorods for various applied anode bias values. Emission current scales as P^3 up to a pulse energy value of 27 nJ (dashed line). (b) Plot of emission current (measured at the cathode) vs applied anode bias for the same Au nanorod array used in (a), at various pulse-energy values. Emission current displays a linear dependence on anode bias at low bias values, consistent with space-charge-limited current as depicted by the color-coordinated lines in the plot. The slope of the linear region of each bias is observed to increase with pulse energy commensurate with the increased area of the emitted sheet of charge expected with increasing pulse energy.

from 3-photon scaling with increasing pulse-energy. The observed deviation from 3-photon scaling with increasing pulse-energy may be attributed to the onset of space-charge-limited current and formation of a virtual cathode, or to a fundamental change in the electron emission mechanism. The scaling of emission current with increasing laser pulse-energy shall be discussed in greater detail in the following section.

Au nanorod arrays with various pitches have been studied in this work. Space-charge effects, as discussed later in the text, are particularly pronounced for higher density arrays with pitches of 200 nm or less due to the associated increase in charge density produced. Consequently, to first understand fundamental emission characteristics in the absence of global space-charge effects, we have investigated low-density arrays of Au nanorods. Figure 2 displays results of the dependence of emission current on both laser intensity (pulse-energy) and on applied anode bias (static DC field).

Figure 2a shows a log–log plot of emission current vs incident laser-pulse energy for a $1\text{ }\mu\text{m}$ pitch square array of Au nanorods. Emission current is seen to scale with the third power of pulse-energy at low intensity consistent with an electron emission mechanism based on the absorption of 3 photons (total energy 4.53–4.77 eV). The work-function (ϕ) of Au has been reported as being in the range of 4.7–5.3 eV.^{29,30} Consequently, the 3-photon scaling observed here is indicative of a work function for the Au nanorod arrays of less than 4.8 eV. A 3-photon scaling for a work function larger than 4.8 eV may also be achieved by photofield emission, whereby an electron from Au is excited to an intermediate state below the vacuum barrier, from which it then tunnels to vacuum.³¹ The emission current is observed to deviate from the 3-photon scaling behavior at a pulse-energy of 27 nJ (12.1 GW/cm² before plasmonic enhancement) irrespective of applied anode bias in the 400–1000 V anode bias range. Were this deviation due to space-charge effects, a shift in the deviation point would be

expected, as its position should depend on anode bias. We can therefore conclude that this deviation instead represents a fundamental change in the emission process, which has been previously attributed to a transition from multiphoton emission to direct strong-field emission in studies of single-tip emitters illuminated with ultrafast infrared pulses.^{31,32} Previously, the Keldysh parameter (γ) has been used to estimate the magnitude of the optical field required to support strong-field emission, where $\gamma < 2$ may describe quasi-static tunneling emission in the strong-field regime, and the transition to tunneling behavior usually occurs in the range $1 < \gamma < 2$.^{33–35} In our system, a 27 nJ pulse-energy is equivalent to an optical field of 0.3 GM^{-1} . A plasmonic field enhancement factor of 40 has been numerically simulated at the Au nanorod surface for a $1\text{ }\mu\text{m}$ pitch square array, as shown in Supporting Information Figure S4. Consequently, an optical field of 12.1 GM^{-1} is expected at the Au nanorod surface or equivalently a Keldysh parameter of $\gamma = 1.5$. Thus, the simulated field-enhancement factor, and the experimentally observed intensity at which deviation occurs from multiphoton emission scaling, supports a transition in the emission mechanism from multiphoton emission to strong-field tunneling at a pulse-energy of 27 nJ.

Figure 2b shows a plot of emission current vs anode bias for 5 different pulse-energy values. This Figure shows that the emission current depends on the anode bias for low bias values, while emission current seems to be independent of anode bias for higher values. The low- and high-bias regimes will be discussed separately below.

In the low-bias regime emission current scales linearly with anode bias, which is consistent with space-charge-limited current (I_{SCL}) as defined by the single sheet model eq 1.³⁶

$$I_{SCL} = \frac{\varepsilon_0 A V f_{laser}}{d} \quad (1)$$

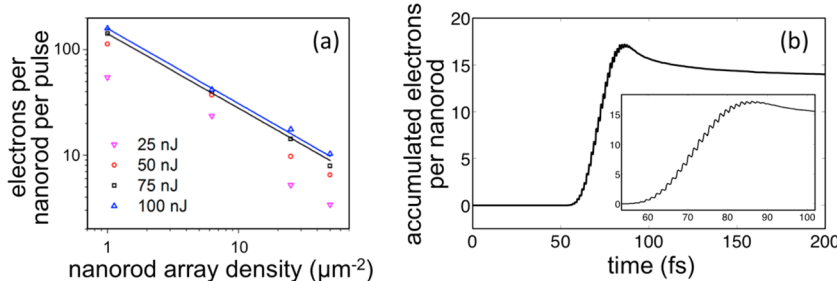


Figure 3. (a) Log–log plot of emitted charge yield per nanorod per pulse vs nanorod array density for four different pulse energies and a fixed anode bias of 1000 V. The color-coordinated lines represent power law fits to the data for 75 and 100 nJ pulse-energy. At high incident pulse-energy the data is observed to follow a power-law, and tends toward a relation given by $Q \sim p^{-0.7}$ (p = array density, Q = charge yield). (b) Simulated temporal evolution of accumulated electron yield per nanorod for a 200 nm pitch square array (25 nanorods μm^{-2}) of Au nanorods illuminated with a 35 fs, 75 nJ pulse centered at 70 fs. The simulation results assume a strong-field tunneling mechanism of emission, which is expected for a 75 nJ pulse-energy. Results predict a charge-yield of 14 electrons per nanorod for a single pulse. Experimentally measured emission matches the predicted yield of 14 electrons per nanorod per pulse. Inset, magnified view of 50–100 fs region showing 1.33 fs period oscillations.

Here ϵ_0 is the vacuum permittivity, A is the area of the sheet of charge emitted, V is the bias voltage, f_{laser} is the repetition rate of the laser (3 kHz), and d is the effective anode–cathode spacing (~ 1 mm). Noticeably, the slope of the linear, current vs anode bias plot is observed to increase with pulse-energy. The slope of the space-charge-limited data in Figure 2b should be related directly to the area of the emitted sheet of charge by eq 1. The area of the sheet of charge should in turn depend on the spatial distribution of laser intensity, which is related directly to the laser pulse-energy for a radially symmetric Gaussian beam. We have found that the observed increase in slope corresponds to the expected increase in the effective area of the laser beam with increasing pulse energy (Supporting Information Figure S9). For example, for a Gaussian beam ($\omega_0 = 76.3 \mu\text{m}$, $\text{fwhm} = 90 \mu\text{m}$), the area of the beam with a threshold optical field of 9 GW cm^{-2} increases by a factor of 2 as the pulse energy is doubled from 37.5 to 75 nJ. Similarly, the slope of the linear region of the plot in Figure 2b increases by a factor of 2 from 0.13 to 0.26 pA V^{-1} , or equivalently from 5.77×10^{-9} to $1.15 \times 10^{-8} \text{ m}^2$, when the pulse energy is increased from 37.5 to 75 nJ (Figure S10, Supporting Information). An optical field of 0.39 GV m^{-1} is equivalent to the peak optical field for a 45 nJ pulse-energy in our system, suggesting that the onset of space-charge-limited current occurs at this incident pulse-energy for the $\sim 1 \text{ MV m}^{-1}$ static field employed in this work. In the high-bias regime, emission current is no longer space-charge-limited and is seen to flatten out. For example, emission current appears to behave independently of the applied anode bias for bias values greater than 600 V at pulse-energy values of 50 nJ (22.5 GW cm^2 before plasmonic enhancement) or less. However, at 75 nJ (33.7 GW cm^2 before plasmonic enhancement), the emission current has not yet saturated at an anode bias of 1 kV, suggesting that the emission current remains influenced by space-charge at this pulse energy.

The effect of nanorod array density on the average charge yield per nanorod, per optical pulse, has also been investigated in this work. The charge yield per nanorod is expected to decrease with increasing array density due to (1) an increased effect of space-charge as the electron sources are pushed closer together, and (2) increased charge screening due to near-field coupling within the nanorod array, resulting in a reduction in nanorod field-enhancement (Supporting Information Figure S4). We have observed emission of more than 200 electrons per nanorod per 35 fs optical pulse from a $1 \mu\text{m}$ pitch, square array, with an incident pulse energy of 120 nJ, and applied anode bias of 1 kV. Moreover, we have observed a power-law relationship between charge-yield and nanorod array density at high pulse-energy values, as shown in Figure 3a. The data does not follow a power-law relation at low incident pulse-energy (< 50 nJ) as emission from high-density arrays is space-charge-limited even at low laser-intensity, while emission from lower density arrays is not. Emission is space-charge-limited for all array densities studied when higher incident pulse-energy (> 75 nJ) is employed. At high incident pulse-energy, the charge yield per nanorod per optical pulse (Q) is related to the array density (p) by the relation $Q = p^{-0.7}$. An array of emitters producing uniform circular disks of charge would be expected to exhibit a relation $Q = p^{-1}$ due to Coulombic effects in the space-charge-limited regime. The observed $Q = p^{-0.7}$ relation may be due to an asymmetric charge distribution produced by the nanorods thus leading to asymmetric space-charge effects in the nanorod arrays. However, screening effects such as those investigated in Supporting Information Figure S4 should also be considered.

Figure 3b presents particle-in-cell simulation results for electron emission from Au nanorods. Briefly, the magnitudes of surface fields are calculated using *COMSOL Multiphysics* within nanometer-scale 3-D cells, as described in Figure 1 and the Supporting Information.

The emission current was then estimated for each surface cell, using the calculated field, by the Fowler-Nordheim approximation for tunneling emission. A detailed explanation of the simulation method is presented in the Supporting Information. The analysis is fulfilled for 200 nm pitch square arrays of Au nanorods illuminated with a 35 fs, 75 nJ pulse centered at a time of 70 fs. Results predict a charge-yield of 14 electrons per nanorod for a single pulse, which agrees well with the experimentally obtained charge-yield of 14 electrons. The temporal evolution of electron yield predicts that the electrons are emitted mainly within the central 20 fs of the pulse. In the rising edge of the plot, fast oscillations are observed with a period of 1.33 fs, which corresponds to a half-cycle of 800 nm light. Consequently, these oscillations are due to the periodic emission from each pole of the dipole emitter as the optical field changes in sign with every half-cycle. The charge-yield from each nanorod is observed to peak at a time of 85 fs before declining slightly to a steady yield of \sim 11 electrons per nanorod. The observed decline in charge-yield is due to the space-charge field causing electrons close to the cathode surface to be pushed back to the substrate. This causes a slow recombination of the electrons, which becomes weaker at stronger anode bias voltages.

To investigate the stability of emission current from Au nanorod arrays, we have measured the emission current from an array of Ti-free Au nanorods, identical to that shown in Figure 1a, for over 5 million pulses (Supporting Information Figure S11). Emission current was measured using an incident pulse-energy of 120 nJ and applied anode bias of 1 kV. The mean emission current was 2.7 nA, with a standard deviation of 30 pA. SEM analysis of the Au nanorod array following extended emission at 120 nJ pulse-energy, showed that a small region of nanorods exhibited damage in a circular area with \sim 1 μ m radius. The observed damage can be attributed to the Gaussian intensity distribution in the laser beam, which may induce field evaporation and electromigration of Au at the center of the Gaussian spot where the optical field is strongest. The slow decay in emission current observed in Supporting Information Figure S11 from 500 to 1800 s may be due to the evolution of damage near the center of the laser spot.

Electron emission from Au nanorod arrays was found to depend strongly on the angle of linear polarization of the incident optical pulse, as depicted in the inset of Figure 4. Emission current was observed to follow a $\cos^6(\theta)$ dependence on polarization angle at low intensity, which is consistent with the 3-photon scaling shown at low intensity in Figure 2a. Additionally, the polarization dependence transitions to a $\cos^2(\theta)$ dependence at higher intensity, which is in good agreement with the observed transition in the electron emission mechanism from that based on multiphoton absorption to quasistatic tunneling emission.

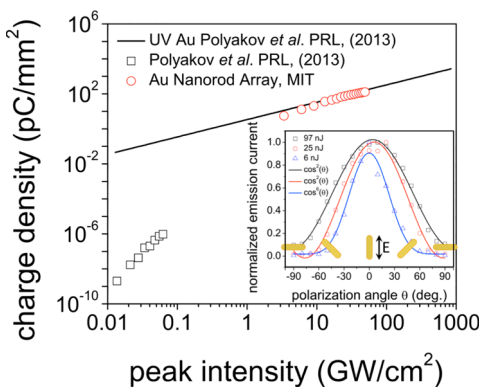


Figure 4. Plot of emitted charge density vs peak laser intensity, for a 200 nm pitch Au nanorod array (red circles) using a 1 kV anode bias and 35 fs optical pulse at a 3 kHz repetition rate. The plot also shows emitted charge density for a plasmonic photocathode developed by Polyakov *et al.* (black squares),¹⁴ which scales with the 4th power of incident laser intensity, suggesting a 4-photon absorption process. The black line represents the charge density emitted from a Au photocathode using UV illumination.¹⁴ Inset, a plot of normalized emission current vs linear polarization angle (θ) at three different values of incident pulse energy. Emission current is highest when the linear polarization is aligned to the long-axis of the nanorod as shown schematically. Emission current follows a $\cos^6(\theta)$ dependence at low pulse-energy, which is equivalent to a 3-photon process. The polarization dependence broadens to a $\cos^2(\theta)$ relation at higher pulse-energy, which is consistent with the transition to strong optical field-emission.

Recently, Polyakov *et al.*¹⁴ have observed photoelectron emission from a plasmonic Au photocathode triggered by 60 fs, linearly polarized pulses, from an 805 nm Ti:sapphire laser. They observed a charge-yield, which scaled as the fourth power of incident laser intensity as represented by the open black squares in Figure 4. Polyakov *et al.* hypothesized that this scaling may continue to laser intensities as high as 50 GW cm^{-2} , at which point their photocathode, which is triggered by an 800 nm laser, may outperform a planar Au photocathode operating under UV illumination (black line Figure 4). In this work, we have seen that a transition from multiphoton emission scaling to strong-field tunneling can occur at a laser intensity of 12.1 GW cm^{-2} (27 nJ pulse-energy), while 3-photon scaling has been measured for intensities as low as $\sim 1 \text{ GW cm}^{-2}$. Consequently, we suggest that plasmonic photocathodes can generate enhanced optical fields sufficient to support strong-field tunneling emission at laser intensities $\sim 10 \text{ GW cm}^{-2}$, and thus that such photocathodes do not display electron emission characteristic of multiphoton absorption at laser intensities for which it was previously predicted.

The maximum charge density emitted from a Au nanorod array photocathode in this work was observed for 200 nm pitch arrays of Ti-free, Au nanorods. Figure 4 shows a plot of charge density emitted per pulse vs peak laser intensity for such an array of Au nanorods (open red circles). Charge-yield from high-density, 200 nm pitch, Au nanorod arrays is still limited

by space-charge effects, even at the highest applied anode bias values used in this work. The observed space-charge suppression of emission current may be alleviated at increased static field. For example, integration of the photocathode within an RF gun capable of producing fields of >10 MV m $^{-1}$ will allow demonstration of a Au nanorod array photocathode, excited by 800 nm light, with a QE that may surpass that of the equivalent UV photoemission process.

In this work, a QE of 1.2×10^{-5} has been measured for 200 nm pitch Au nanorods illuminated with 800 nm light at an intensity of 10 GW cm $^{-2}$ from the data in Figure 4. The QE for Au illuminated with UV light (266 nm) has been reported as 4.7×10^{-5} .³⁷ The transmitted laser intensity was measured as $\sim 90\%$ for a 200 nm pitch array of Au nanorods at the laser focus for a laser intensity of 34 GW/cm 2 . Thus, an internal QE can be calculated as 1.2×10^{-4} considering $\sim 10\%$ of the incident photons as scattering from the nanorod array to produce photoelectrons. When the 10% power conversion efficiency of 800 nm wavelength light to 266 nm wavelength light by third harmonic generation, and the factor of 3 difference in energy between the IR and UV light are taken into consideration, plasmonic Au nanorod arrays triggered by 800 nm wavelength light can be considered as ~ 100 times more efficient than UV-triggered bulk Au photocathodes. Furthermore, as has been discussed, application of an increased static bias to lift

the space-charge limit would further improve the QE for this system.

CONCLUSIONS

We propose that the photocathodes developed in this work may be sufficiently robust for use in XFEL systems when operated using a laser-intensity below the damage threshold (~ 45 GW cm $^{-2}$) and under a sufficiently strong static-field (>10 MV m $^{-1}$). Under such conditions, Au nanorod arrays triggered by ultrafast pulses of 800 nm light, may outperform equivalent UV-triggered Au photocathodes, while also offering nanostructuring of the electron pulse produced from such a cathode, which is of interest for future XFEL development where nanostructured electron pulses may facilitate more efficient and brighter XFEL radiation. Moreover, Au nanorods triggered by 800 nm light at intensities above 12 GW cm $^{-2}$ may emit electrons by a strong-field tunneling mechanism, and thus may support production of attosecond electron bursts, which are key to the development of attosecond science. Further investigations are required to maintain the initial levels of confinement of electrons in both space and time possible at the emitter surface, into a propagating nanostructured pulse-train. As a result, the Au nanorod photocathodes developed in this work represent an additional step toward the development of analytical tools with attosecond temporal resolution.

METHODS

Nanorod Array Fabrication. Nanorod array photocathodes were fabricated on 10 mm \times 10 mm sapphire or Si (n-type, 1–10 $\Omega\cdot\text{cm}$) dies. The transparent sapphire substrate was chosen to facilitate transmission spectroscopy measurements. A 50–80 nm layer of indium-doped tin oxide (ITO) was deposited on the substrate to function as the cathode electrode. The low refractive index of ITO was favored for photocathode application (see Supporting Information). This conducting film also negated issues associated with substrate charging, common to electron-beam lithography on insulating substrates such as sapphire. ITO layers were deposited by RF magnetron sputtering at an RF power of 80 W and substrate temperature of 100 °C, resulting in a deposition rate of 0.5 Å s $^{-1}$. A 70 nm film of PMMA (2% 950k PMMA in anisole, *MicroChem Corp.*) was then deposited by spin coating at 2 krpm and soft-baked at 180 °C for 2 min. Nanorod array patterns were defined by electron-beam lithography using an Elionix F-125 EBL system. The electron energy for lithography was 125 keV, electron beam current was 0.5 or 1 nA, and typical exposure dose was 800 electron/nm 2 . Exposed PMMA was developed in 3:1 IPA:MIBK at 0 °C for 30 s with constant agitation and dried under dry flowing N₂ gas. Low temperature development was used to improve the resolution of electron-beam lithography. Metals were then deposited via electron-beam evaporation. Au nanorod arrays prepared with a 3 nm Ti adhesion layer used a Au evaporation rate of 0.5 Å s $^{-1}$ in the vacuum chamber ($\sim 10^{-6}$ mbar), while for Au nanorod arrays prepared without a Ti layer, Au was evaporated at a slower rate of 0.1 Å s $^{-1}$ to reduce stress in the deposited Au layer and prevent delamination of Au nanorods from the substrate. Metal lift-off was performed in *n*-methylpyrrolidone (NMP) at 55 °C for approximately 60 min during which the samples were

gently rinsed intermittently with flowing NMP. Ultrasonication was not used during lift-off as it was shown to create vacancy defects in the nanorod arrays prepared with a Ti adhesion layer, and caused delamination of almost the entire array in the case of nanorods prepared without an adhesion-promoting layer. After lift-off, the samples were rinsed with acetone and isopropyl alcohol. Gentle O₂ plasma ashing (50 W, 60 s) was applied to remove residual resist and solvents immediately prior to photoelectron emission measurements. No observable damage of Au nanorods due to O₂ plasma was detected in SEM images and photoemission data. The fabrication process is illustrated in Figure S7 in the Supporting Information.

Electron Emission Measurements. Photoelectron emission from Au nanorod arrays was triggered with 35 fs laser pulses with a central wavelength of 800 nm and a spectral bandwidth of 38 nm at a 3 kHz repetition rate from a regeneratively amplified titanium sapphire oscillator seed. A Thor Laboratories S322C thermal power sensor was used to measure the laser power. The light was linearly polarized and the polarization angle was controlled *via* a half-wave plate as required. The light was normally incident on the nanorod arrays *via* front illumination. The pulsed light was focused to a 90 μm (fwhm) spot at the nanorod arrays. The photocathode samples were mounted in a high-vacuum chamber (10^{-8} Torr). A schematic of the measurement setup is shown in Supporting Information Figure S8. A static DC bias was applied to an Al ring-anode. The ring had a 6.35 mm outer diameter, a 2.286 mm inner diameter, and a thickness of 0.508 mm. The anode was placed on a 60 μm thick mica insulating spacer thus isolating the anode from the cathode. The ring-anode, together with the insulator, was placed directly on the surface of photocathode samples with Au nanorod arrays aligned at the center of the ring. A Keithley

237 source measurement unit (SMU) was used to bias the anode with voltages up to 1.1 kV and measure the anode current. A Keithley 6485 picoammeter was used to measure the cathode current. Unless otherwise stated the current measurements presented in the main text are those recorded at the cathode. Secondary electron generation at the anode can lead to higher measured current values at the anode than the cathode.

A schematic of the ring-anode–cathode configuration as well as the electrostatic simulation result on a cross-section normal to the photocathode substrate surface is shown in Supporting Information Figure S9. Materials of different structures are labeled. The cathode substrate (ITO) is grounded and the anode (Al) is biased at +1000 V. The color scale stands for electric field strength and is saturated at 2 MV/m. The black arrows indicate the direction of local electric field. It can be seen at the position of Au nanorod arrays ($x = 0, y = 0$) that the electric field strength is approximately 1 MV/m and uniform, while its direction is approximately normal to the cathode surface.

Details of electromagnetic and electron emission simulations are included in the Supporting Information.

Conflict of Interest: The authors declare no competing financial interest.

Acknowledgment. The authors acknowledge financial support from DARPA under contract N66001-11-1-4192, and the Gordon and Betty Moore Foundation. The authors would like to acknowledge Dr. Rafael Jaramillo for assistance with ITO deposition, Mr. Mark Mondol, and Mr. Jim Daley of the NanoStructures Laboratory at MIT for assistance with fabrication and Dr. Michael Swanwick, Dr. Yoel Yang and Mr. William Putnam, for useful discussions.

Supporting Information Available: Additional field-enhancement simulations, results of spectroscopic characterization of nanorod arrays and experimental details. This material is available free of charge via the Internet at <http://pubs.acs.org>.

REFERENCES AND NOTES

- Nie, S.; Emory, S. R. Probing Single Molecules and Single Nanoparticles by Surface-Enhanced Raman Scattering. *Science* **1997**, *275*, 1102–1106.
- Imura, K.; Nagahara, T.; Okamoto, H. Near-Field Optical Imaging of Plasmon Modes in Gold Nanorods. *J. Chem. Phys.* **2005**, *122*, 154701–154705.
- Christopher, P.; Xin, H.; Linic, S. Visible-Light-Enhanced Catalytic Oxidation Reactions on Plasmonic Silver Nanostructures. *Nat. Chem.* **2011**, *3*, 467–472.
- Zhao, Y.; Alù, A. Tailoring the Dispersion of Plasmonic Nanorods to Realize Broadband Optical Meta-Waveplates. *Nano Lett.* **2013**, *13*, 1086–1091.
- Zhao, Y.; Belkin, M. A.; Alù, A. Twisted Optical Metamaterials for Planarized Ultrathin Broadband Circular Polarizers. *Nat. Commun.* **2012**, *3*, 870.
- Fafarman, A. T.; Hong, S.-H.; Caglayan, H.; Ye, X.; Diroll, B. T.; Paik, T.; Engheta, N.; Murray, C. B.; Kagan, C. R. Chemically Tailored Dielectric-to-Metal Transition for the Design of Metamaterials from Nanoimprinted Colloidal Nanocrystals. *Nano Lett.* **2013**, *13*, 350–357.
- Mayer, K. M.; Hafner, J. H. Localized Surface Plasmon Resonance Sensors. *Chem. Rev.* **2011**, *111*, 3828–3857.
- Anker, J. N.; Hall, W. P.; Lyandres, O.; Shah, N. C.; Zhao, J.; Van Duyne, R. P. Biosensing with Plasmonic Nanosensors. *Nat. Mater.* **2008**, *7*, 442–453.
- Lal, S.; Link, S.; Halas, N. J. Nano-Optics from Sensing to Waveguiding. *Nat. Photonics* **2007**, *1*, 641–648.
- Koller, D. M.; Hohenau, A.; Ditlbacher, H.; Galler, N.; Reil, F.; Ausseneegg, F. R.; Leitner, A.; List, E. J. W.; Krenn, J. R. Organic Plasmon-Emitting Diode. *Nat. Photonics* **2008**, *2*, 684–687.
- Volpe, G.; Noack, M.; Aćimović, S. S.; Reinhardt, C.; Quidant, R. Near-Field Mapping of Plasmonic Antennas by Multiphoton Absorption in Poly(methyl methacrylate). *Nano Lett.* **2012**, *12*, 4864–4868.
- Dombi, P.; Horl, A.; Racz, P.; Marton, I.; Trugler, A.; Krenn, J. R.; Hohenester, U. Ultrafast Strong-Field Photoemission from Plasmonic Nanoparticles. *Nano Lett.* **2013**, *13*, 674–678.
- Li, R. K.; To, H.; Andonian, G.; Feng, J.; Polyakov, A.; Scoby, C. M.; Thompson, K.; Wan, W.; Padmore, H. A.; Musumeci, P. Surface-Plasmon Resonance-Enhanced Multiphoton Emission of High-Brightness Electron Beams from a Nanostructured Copper Cathode. *Phys. Rev. Lett.* **2013**, *110*, 074801.
- Polyakov, A.; Senft, C.; Thompson, K. F.; Feng, J.; Cabrini, S.; Schuck, P. J.; Padmore, H. A.; Peppernick, S. J.; Hess, W. P. Plasmon-Enhanced Photocathode for High Brightness and High Repetition Rate X-Ray Sources. *Phys. Rev. Lett.* **2013**, *110*, 076802.
- Aeschlimann, M.; Schmuttenmaer, C. A.; Elsayed-Ali, H. E.; Miller, R. J. D.; Cao, J.; Gao, Y.; Mantell, D. A. Observation of Surface Enhanced Multiphoton Photoemission from Metal Surfaces in the Short Pulse Limit. *J. Chem. Phys.* **1995**, *102*, 8606–8613.
- Dowell, D. H.; Bazarov, I.; Dunham, B.; Harkay, K.; Hernandez-Garcia, C.; Legg, R.; Padmore, H.; Rao, T.; Smedley, J.; Wan, W. Cathode R&D for Future Light Sources. *Nucl. Instrum. Methods Phys. Res., Sect. A* **2010**, *622*, 685–697.
- Barletta, W. A.; Bisognano, J.; Corlett, J. N.; Emma, P.; Huang, Z.; Kim, K.-J.; Lindberg, R.; Murphy, J. B.; Neil, G. R.; Nguyen, D. C.; et al. Free Electron Lasers: Present Status and Future Challenges. *Nucl. Instrum. Methods Phys. Res., Sect. A* **2010**, *618*, 69–96.
- Freund, H. P.; Nguyen, D. C.; Carlsten, B. Three-Dimensional Analysis of Prebunched Electron Beams in an X-Ray Free-Electron Laser. *Phys. Rev. Spec. Top—Accel. Beams* **2012**, *15*, 030704.
- Graves, W. S.; Kärtner, F. X.; Moncton, D. E.; Piot, P. Intense Superradiant X-rays from a Compact Source Using a Nanocathode Array and Emittance Exchange. *Phys. Rev. Lett.* **2012**, *108*, 263904.
- Nagel, P. M.; Robinson, J. S.; Harteneck, B. D.; Pfeifer, T.; Abel, M. J.; Prell, J. S.; Neumark, D. M.; Kaindl, R. A.; Leone, S. R. Surface Plasmon Assisted Electron Acceleration in Photoemission from Gold Nanopillars. *Chem. Phys.* **2013**, *414*, 106–111.
- Douillard, L.; Charra, F.; Korczak, Z.; Bachelot, R.; Kostcheev, S.; Lerondel, G.; Adam, P.-M.; Royer, P. Short Range Plasmon Resonators Probed by Photoemission Electron Microscopy. *Nano Lett.* **2008**, *8*, 935–940.
- Halas, N. J.; Lal, S.; Chang, W.-S.; Link, S.; Nordlander, P. Plasmons in Strongly Coupled Metallic Nanostructures. *Chem. Rev.* **2011**, *111*, 3913–3961.
- Knight, M. W.; Wu, Y.; Lassiter, J. B.; Nordlander, P.; Halas, N. J. Substrates Matter: Influence of an Adjacent Dielectric on an Individual Plasmonic Nanoparticle. *Nano Lett.* **2009**, *9*, 2188–2192.
- Wu, Y.; Nordlander, P. Finite-Difference Time-Domain Modeling of the Optical Properties of Nanoparticles near Dielectric Substrates. *J. Phys. Chem. C* **2010**, *114*, 7302–7307.
- Schweikhard, V.; Grubisic, A.; Baker, T. A.; Thomann, I.; Nesbitt, D. J. Polarization-Dependent Scanning Photoionization Microscopy: Ultrafast Plasmon-Mediated Electron Ejection Dynamics in Single Au Nanorods. *ACS Nano* **2011**, *5*, 3724–3735.
- Zhang, S.; Bao, K.; Halas, N. J.; Xu, H.; Nordlander, P. Substrate-Induced Fano Resonances of a Plasmonic Nanocube: A Route to Increased-Sensitivity Localized Surface Plasmon Resonance Sensors Revealed. *Nano Lett.* **2011**, *11*, 1657–1663.
- Hutter, T.; Elliott, S. R.; Mahajan, S. Interaction of Metallic Nanoparticles with Dielectric Substrates: Effect of Optical Constants. *Nanotechnology* **2013**, *24*, 035201.
- Habteyes, T. G.; Dhuey, S.; Wood, E.; Gargas, D.; Cabrini, S.; Schuck, P. J.; Alivisatos, A. P.; Leone, S. R. Plasmon Damping and Molecular Linker as a Nondamping Alternative. *ACS Nano* **2012**, *6*, 5702–5709.
- Hansen, W. N.; Johnson, K. B. Work Function Measurements in Gas Ambient. *Surf. Sci.* **1994**, *316*, 373–382.
- Lide, D. R. *CRC Handbook of Chemistry and Physics*; Lide, D. R., Ed.; Internet V; Boca Raton, FL, 2005.

31. Hommelhoff, P.; Sortais, Y.; Aghajani-Talesh, A.; Kasevich, M. A. Field Emission Tip as a Nanometer Source of Free Electron Femtosecond Pulses. *Phys. Rev. Lett.* **2006**, *96*, 077401.
32. Bormann, R.; Gulde, M.; Weismann, A.; Yalunin, S.; Ropers, C. Tip-Enhanced Strong-Field Photoemission. *Phys. Rev. Lett.* **2010**, *105*, 147601.
33. Keathley, P. D.; Sell, A.; Putnam, W. P.; Guerrera, S.; Velasquez-Garcia, L.; Kaertner, F. X. Strong-Field Photoemission from Silicon Field Emitter Arrays. *Ann. Phys. (Berlin, Ger.)* **2012**, *525*, 144–150.
34. Krüger, M.; Schenk, M.; Hommelhoff, P. Attosecond Control of Electrons Emitted from a Nanoscale Metal Tip. *Nature* **2011**, *475*, 78–81.
35. Swanwick, M. E.; Keathley, P. D.; Fallahi, A.; Krogen, P. R.; Laurent, G.; Moses, J.; Kärtner, F. X.; Velasquez-Garcia, L. F. Nanostructured Ultrafast Silicon-Tip Optical Field-Emitter Arrays. *Nano Lett.* **2014**, *14*, 5035–5043.
36. Valfells, A.; Feldman, D. W.; Virgo, M.; O'Shea, P. G.; Lau, Y. Y. Effects of Pulse-Length and Emitter Area on Virtual Cathode Formation in Electron Guns. *Phys. Plasmas* **2002**, *9*, 2377–2382.
37. Srinivasan-Rao, T.; Fischer, J.; Tsang, T. Photoemission Studies on Metals Using Picosecond Ultraviolet Laser Pulses. *J. Appl. Phys.* **1991**, *69*, 3291–3296.